Red-Fluorescing Paramagnetic Conjugated Polymer Nanoparticles—Triphenyl Methyl Radicals as Monomers in C−C Cross-Coupling Dispersion Polymerization

Lisa Chen, Tamara Rudolf, Rémi Blinder, Nithin Suryadevara, Ashley Dalmeida, Philipp J. Welscher, Markus Lamla, Mona Arnold, Ulrich Herr, Fedor Jelezko, Mario Ruben, and Alexander J. C. Kuehne*
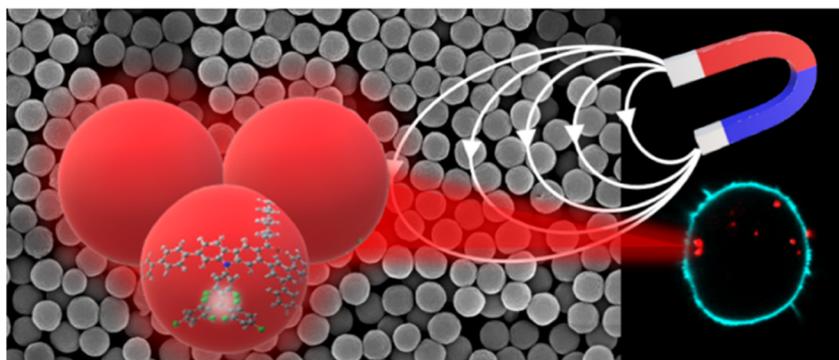
ABSTRACT: We report the synthesis of conjugated polymer nanoparticles carrying stable luminescent radical units. These monodisperse conjugated radical nanoparticles can be tuned in their diameter over several hundred nanometers. They are stable in aqueous medium and highly luminescent in the red and near-infrared spectra, representing a powerful future tool for bioimaging. Moreover, the polymer nanoparticles exhibit paramagnetic properties, making them highly suitable for dual-mode optical and magnetic resonance imaging. In this study, we investigate their synthesis as well as optical and magnetic properties, and use quantum mechanical calculations to elucidate the effect of the conjugated polymer backbone and electron-withdrawing substituents on the electronic properties of the open-shell molecule in the polymer network of the particles.

1. INTRODUCTION

Light-emitting radicals that have been functionalized with electron donor moieties represent an interesting class of open-shell materials with high photoluminescence quantum yield[1] (ϕ) and potential susceptibility to magnetic fields.[2−4] The doublet spin properties in these open-shell emitters evade the unfavorable formation of dark triplet states, thus making luminescent radicals promising emitters for next-generation organic light-emitting devices.[5−7] Besides their excellent optical performance, the unpaired electron of these radicals also introduces exceptional conductivity and magnetic properties that are interesting for their application in spintronics,[8] batteries,[9] organic field-effect transistors,[10] organic magnets,[11−13] and imaging applications.[14] However, for most relevant imaging techniques, the radical species needs to be transferred into polar solvents such as water. Here, the excited charge-transfer (CT) state, from which emission occurs becomes stabilized by the polar medium and the oscillator strength drops significantly, deteriorating ϕ of the luminescent radicals. By contrast, locally excited (LE) radical emitters exhibit low quantum yields per se, apart from being hardly

soluble in polar solvents. One solution for this problem is to treat the light-emitting radicals in the form of nanoparticles. Tris(trichlorophenyl)methyl (TTM) radicals have previously been shaped into nanoparticles simply by reprecipitation into a bad solvent, leading to a broad size distribution of particles that suffer from aggregation.[15] This problem can be prevented by encapsulating crystallites of TTM-based radicals into the core of block-copolymer micelles.[16] When TTM is functionalized with 3-bromo-*N*-carbazole as a donor (CzBr$_1$-TTM), block-copolymer stabilized nanoparticles are obtained, with a reported ϕ of up to 18.6% as compared to the TTM particles with around 2%. When the nanoparticles consist of pure aggregated or crystallized radicals, the observed fluorescence is dominated by excimer emission and aggregation-induced
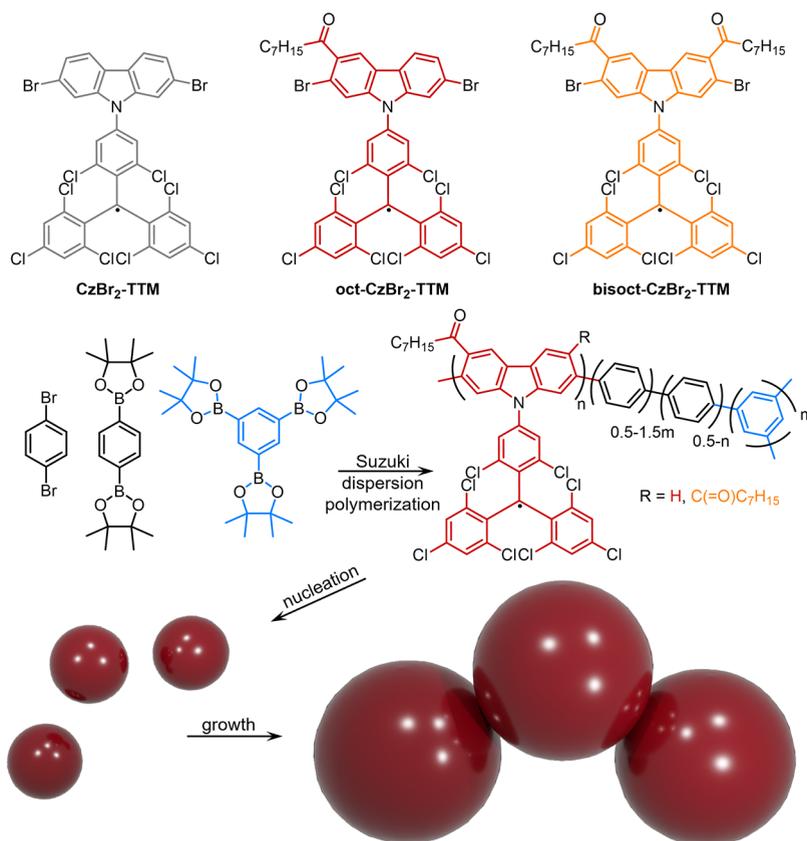
Figure 1. Schematic illustration of the employed monomers and the mechanism of dispersion polymerization to obtain monodisperse CPNs.

quenching can be observed. Thus, in both studies, the best emission characteristics are observed when the radical is doped into a matrix of their closed-shell equivalent to improve the fluorescence properties of the particles. To gain better control over the inter-radical spacing, it would be beneficial to incorporate the radical emitters into a polymer backbone, facilitating better inter-radical spacing and a more amorphous particle morphology. This approach would potentially increase the absorption cross-section, while facilitating energy transfer from an absorbing backbone into the radical emitter units. Such a process could be realized by incorporating the radical unit into conjugated polymer nanoparticles. Typically, conjugated polymers are functionalized with solubilizing alkyl groups to prevent aggregation in solution and emission quenching in the solid state. Conjugated polymer nanoparticles (CPNs) can be obtained through polymerization of soluble monomers in a solvent, in which the resulting desired polymer is insoluble. A variety of different preparation methods has been brought forward to control the sizes of the CPNs;[17−21] however, only dispersion polymerization[22−27] yields particles of sufficiently low dispersity to allow their application in the fields of photonics[28,29] and bioimaging.[30−34] CPNs have been reported to exhibit high photostability, as well as excellent biocompatibility.[35−37] However, to date, no open-shell monomers have been employed in these dispersion polymerizations, and it remains unknown whether the radical nature could survive the reaction conditions of transition-metal-mediated C−C cross-coupling reactions. Incorporation of open-shell monomers into CPNs could open up completely new particle features and render CPNs paramagnetic. Such luminescent radicals would exhibit unique electronic and

magnetic characteristics, induced by the doublet spin configuration. These all-organic radical CPNs could present highly promising building blocks for photonic devices that are responsive to external electric and magnetic fields, as well as biomedical imaging probes with contrast in optical and magnetic imaging techniques.

Here, we synthesize monodisperse conjugated polymer particles with a Cz-TTM-based radical comonomer. We show that the unpaired electron on the TTM remains intact during Suzuki−Miyaura C−C cross-coupling polymerization. We verify the applicability of this approach by varying the particle size and characterizing the stability as well as the optical and magnetic properties of this new class of conjugated polymer nanoparticles. Moreover, we show that the particles remain fluorescent with ϕ of up to 5.3% also in aqueous medium.

2. RESULTS AND DISCUSSION

2.1. Synthesis and Characterization of the Open-Shell Monomer.
To incorporate open-shell TTM motifs into CPNs, we first have to develop a suitable TTM monomer that can engage in transition-metal-mediated C−C cross-coupling, for example, Suzuki−Miyaura coupling. The stable and luminescent 2,7-dibromo-4-N-2,6-(dichlorophenyl)bis(2,4,6,-trichlorophenyl)methyl (**CzBr₂-TTM**) radical carrying two bromide groups appears as a favorable choice for an open-shell monomer (see Figure 1). Its synthesis is straightforward by coupling commercially available 2,7-dibromo-carbazole with TTM.[38] Unfortunately, this rigid and nonpolar monomer is hardly soluble in alcohols, which is a requirement to obtain monodisperse nanoparticles during dispersion polymerization.
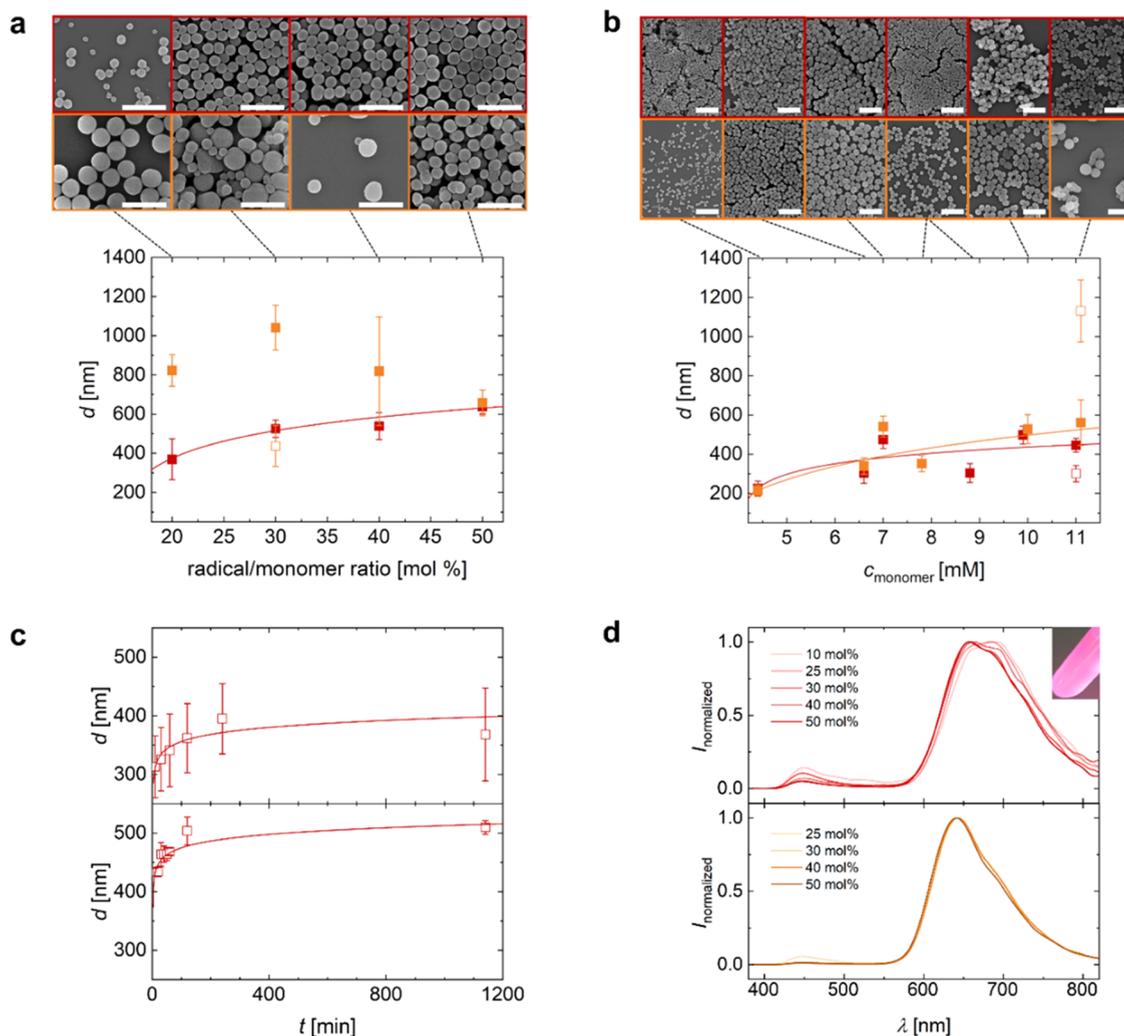
Figure 2. (a) Particle diameter synthesized from **oct-CzBr$_2$-TTM** (red) and **bisoct-CzBr$_2$-TTM** (orange) versus the initial ratio of the open-shell monomer. The overall monomer concentration is kept constant at 7.3 mM. The SEM images show the improving shape and monodispersity with an increasing amount of radical monomer. An increase in particle size is observed for **oct-CzBr$_2$-TTM** as a monomer, while no clear trend can be derived for the CPNs synthesized from **bisoct-CzBr$_2$-TTM**. The scale bars in the SEM images represent 2 μm. (b) The particle diameter versus initial monomer loading at a constant initial radical ratio of 25 mol % **oct-CzBr$_2$-TTM** and **bisoct-CzBr$_2$-TTM**, respectively. At monomer concentrations above 9.9 mM, secondary nucleation occurs; consequently, bidisperse CPNs are obtained. This is shown by the empty symbols, representing the diameter of the particles formed by secondary nucleation. The scale bars in the SEM images represent 2 μm. (c) Evolution of the particle size over time. The overall monomer concentration is set to 7.3 mM with 25 mol % of **oct-CzBr$_2$-TTM**. The data in the top graph is collected from the SEM images, while the data in the bottom graph is obtained from DLS measurements. Both data sets show a similar course for the particle growth, but the values differ by ca. 100 nm, indicating that the particle will be slightly swollen when dispersed. (d) Photoluminescence spectra of CPN dispersions in 1-PrOH synthesized with different initial radical monomer contents of **oct-CzBr$_2$-TTM** and **bisoct-CzBr$_2$-TTM** in mol %. The inset shows a photograph of a radical CPN dispersion under UV light synthesized with the same parameters as used for the kinetic study.

The introduction of flexible octanoyl groups at the 3 and 6 positions of the carbazole moiety by Friedel−Crafts acylation improves the solubility of the molecules in alcohols significantly (see Scheme S1). During the acylation reaction, we obtain the desired open-shell monomer with one (**oct-CzBr$_2$-TTM**) and two octanoyl chains (**bisoct-CzBr$_2$-TTM**) (see Figure 1). The two products can be separated by column chromatography, delivering both molecules as pure compounds. It is found that the bis- and mono-acylated molecules are soluble in 1-propanol, the solvent of choice for dispersion polymerizations of CPNs. Because of the electron-withdrawing nature of octanoyl substituents, the emission wavelength of the **CzBr$_2$-TTM**-based monomers is shifted to higher energies with an increasing number of acyl groups. While the small

amount of **CzBr$_2$-TTM** that is soluble in 1-propanol emits at 685 nm, the emission of **bisoct-CzBr$_2$-TTM** is hypsochromically shifted to 615 nm (see Figure S1a). The emission of the **CzBr$_2$-TTM**-based radicals is strong with ϕ of around 40% (in cyclohexane) and in the orange to deep red spectral region.[38] The introduction of acyl chains to the carbazole unit does not affect the quantum yield significantly; only a slight decrease in ϕ to 32 and 23%, respectively, is observed. The photoluminescence lifetime (τ) decreases considerably with the attachment of the acyl units. While **CzBr$_2$-TTM** has a lifetime of 36 ns in toluene solution, the lifetimes of **bisoct-CzBr$_2$-TTM** and **oct-CzBr$_2$-TTM** reduce to 13.7 and 3.9 ns in 1-propanol solution, respectively (see Figure S3a). All molecules exhibit a monoexponential fluorescence decay. The decrease in

τ compared to **CzBr$_2$-TTM** will derive from the additional electron-withdrawing nature of the octanoyl chains, which reduces the CT character of the excited state. CT states are common for donor−acceptor-type molecules like carbazole-substituted TTMs and are known for their long τ. However, **oct-CzBr$_2$-TTM** exhibits an even shorter lifetime than **bisoct-CzBr$_2$-TTM**, which is not in line with the CT state argument. A second mechanism, namely, the reduction in symmetry for the mono-acylated molecule, is most likely evoking this significant reduction in τ.[39,40] The reduction in symmetry from C$_{2v}$ to C$_1$ causes formerly forbidden transitions by the optical selection rules to become symmetry-allowed, thus leading to a decrease in the photoluminescence lifetime.

2.2. Particle Synthesis and Characterization. We perform dispersion polymerization with both the mono- and the bis-octanoylated radical monomers and adapt the previously reported protocols to our open-shell monomers.[22] As comonomers, we employ phenylenes with bromine and boronic acid functionalities (see Figure 1). These monomers do not absorb or emit in the visible region, thus preventing spectral overlap of the resulting backbone with the red emission of the open-shell radical emitters. We add 1,3,5-tris[(pinacolato)boryl]benzene as a cross-linker to create an immiscible 3-dimensionally connected network inside of the particles. With this set of comonomers, we conduct Suzuki-type dispersion polymerization in accordance with previously established reaction conditions using tetrakis-(triphenylphosphine)palladium(0) as the catalyst and potassium *tert*-butoxide as the base.[22] Poly(vinylpyrrolidone-*co*-vinyl acetate) and Triton X-45 are added as stabilizers, thus avoiding aggregation of nuclei and particles during as well as after polymerization.[22] All reagents are dissolved in 1-propanol under an inert argon atmosphere and heated to 70 °C to initiate the reaction. At a critical molecular weight, the growing polymer chains become insoluble in the solvent and phase separation occurs, resulting in the nucleation of particles. Subsequent particle growth is facilitated by a combination of surface polymerization and crosslinking as well as condensation of polymer chains formed in solution onto the surface of the growing particles (see Figure 1).[23,41]

To gain full control over the reaction and to tune the properties of the obtained CPNs, we vary the radical content as well as the combined monomer concentration in the reaction mixture. An increase in the particle size is observed for higher ratios of the open-shell **oct-CzBr$_2$-TTM** to the other monomers (see Figure 2a). At an overall constant monomer concentration of 7.3 mM and less than 20 mol % of **oct-CzBr$_2$-TTM**, no CPNs are formed. At 20 mol %, few particles form; however, these are polydisperse. Only at **oct-CzBr$_2$-TTM** contents greater than 20 mol % do the resulting CPNs become monodisperse. Especially, particles with the highest possible amount of 50 mol % radical are perfectly spherical with a dispersity of only Đ = 0.05 (d = 638 ± 36 nm), allowing them to assemble into hexagonally arranged colloidal crystals (see the inset of Figure 2a). Overall, we can vary the diameter d of the obtained monodisperse particles across a range of ca. 250 nm using ratios between 20 and 50 mol % (see Figure 2a). This indicates that if higher radical ratios are applied, the addition of the open-shell monomer evokes phase separation to occur at an earlier stage of the reaction—a prerequisite for uniform particle nucleation and growth. The particle size is also dependent on the overall monomer concentration. Using a constant **oct-CzBr$_2$-TTM** to the overall monomer ratio of 25

mol %, the size of the resulting particles can be doubled by increasing the combined monomer loading from 4.4 to 11 mM (see Figure 2b). Concentrations below 7 mM deliver CPNs that tend to aggregate due to their high surface-to-volume ratio at such small sizes. By contrast, at very high concentrations of 11 mM and above, apparently secondary nucleation occurs, resulting in bidisperse or polydisperse sets of particles. The best results for monodisperse CPNs are obtained at monomer loadings between 7 and 9.9 mM (see Figure 2b). We carry out the same experiments using **bisoct-CzBr$_2$-TTM** as a comonomer for CPN synthesis. However, the particles obtained from this comonomer are not as monodisperse as those made using the mono-acylated **oct-CzBr$_2$-TTM** comonomer. The reason for this is most likely found in the better solubility of **bisoct-CzBr$_2$-TTM** compared to **oct-CzBr$_2$-TTM**. Mediated by the second octanoyl chain, polymers with incorporated **bisoct-CzBr$_2$-TTM** will exhibit augmented solubility, and thus phase separation and nucleation will be delayed and occur at higher molecular weights. In a step-growth polymerization, this is associated with less well-controlled particle growth, leading to irregular size and shape of the particles, as observed in Figure 2a. For the series of particles synthesized with an overall combined monomer concentration of 7.3 mM, spherical and monodisperse particles could only be obtained for some isolated radical concentrations, making it difficult to describe a trend for their change in size dependent on the radical concentration. Similar to the monooctanoyl radical monomer, the bifunctionalized **bisoct-CzBr$_2$-TTM** delivers larger particles for higher overall monomer loadings. Concentrations from 6.6 to 10 mM deliver a steady increase of the particle diameter. Higher concentrations again entail secondary nucleation, leading to bi- and polydisperse distributions of particle diameters (see Figure 2b).

To investigate the reaction kinetics more closely, we focus on **oct-CzBr$_2$-TTM** and perform the reaction with a combined monomer concentration of 7.3 mM and a radical ratio of 25 mol %. We take aliquots from the reaction mixture at dedicated points in time. The aliquots are quenched in cold 1-propanol to stop the polymerization. After purification of the aliquots by repeated centrifugation and redispersion in fresh 1-propanol, their particle diameters are determined in the dispersed state by dynamic light scattering (DLS) and in the solid state by scanning electron microscopy (SEM). Both characterization methods describe a similar trend for the growth of the particles (see Figure 2c). Nuclei will have formed almost immediately, and we observe the steady growth of the particle diameter over an interval of 300 min. We consider the reaction to be completed at around 100 min, but we record an additional timepoint after 24 h to display that marginal to no change in d occurs, indicating that the reaction is indeed over after $t \sim 100$ min (see Figure 2c). Interestingly, the DLS data display a particle size that is around 100 nm bigger compared to the diameters found in the SEM images. Typically, DLS gives greater values than SEM analysis simply because the Stokes−Einstein diameter determined by DLS includes the solvation envelope of the particles.[42] However, the difference of 100 nm in d cannot be coming from this solvation effect alone, indicating that the particles will be slightly swollen in 1-propanol, which also adds to the diameter (see Figure 2c).

Regardless of their size, all particles exhibit red photoluminescence when illuminated with light of suitable excitation wavelengths. The photoluminescence spectra of the particle dispersions in 1-propanol made from **oct-CzBr$_2$-TTM** exhibit
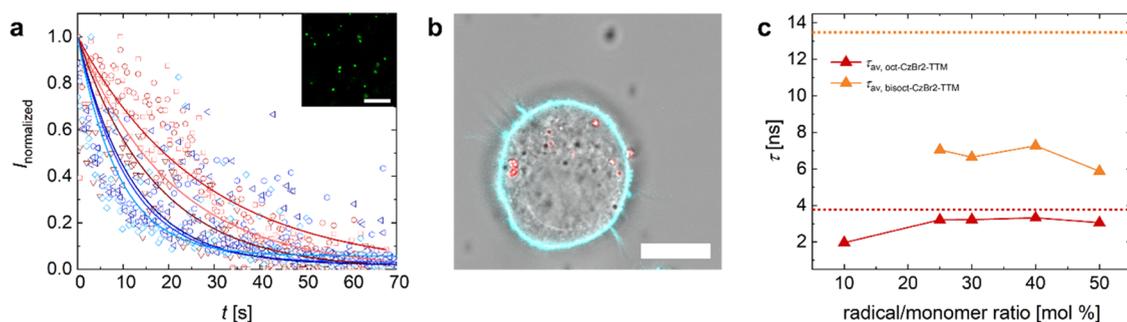
Figure 3. (a) Photoluminescence intensity of radical CPNs made from 50 mol % **oct-CzBr₂-TTM** (red) and latex reference particles loaded with commercial red dye (blue) as a function of time. Both particle dispersions are illuminated with a 5.1 mW CW-laser at 561 nm and three distinctive particles of both batches are recorded over time. The straight lines show an exponential fit of the data. The inset shows a confocal image of the stable aqueous dispersion of the luminescent open-shell CPNs. (b) Confocal image showing the uptake of the red-fluorescing CPNs by macrophages labelled in blue after 3 h of incubation. The scale bars in the confocal images represent 10 μm. (c) Photoluminescence lifetime of radical CPNs with different initial radical loadings. The dotted lines are the lifetimes of the monomers **oct-CzBr₂-TTM** (red) and **bisoct-CzBr₂-TTM** (orange).

two bands when excited at 380 nm: a weak band at 450 nm and a strong signal between 655 and 690 nm (see Figure 2d). The blue signal can either derive from the polymer backbone emission or originate from the emission of the closed-shell **oct-CzBr₂-TTM-H** monomer that could form during polymerization. However, the fact that the blue emission diminishes with increasing loading of the radical comonomers indicates that the emission will not come from the closed-shell **oct-CzBr₂-TTM-H**, as then this band should rise. Instead, the blue emission band decreases indicating that it stems from incomplete energy transfer from the backbone to the radical. This shows that the TTM-based radical monomers are stable during dispersion polymerization and the open-shell emitters are indeed incorporated into the CPN. The combined blue emission of the backbone and the red emission from the radical unit at low radical ratios appears pink to the naked eye (see the inset Figure 2d). The red emission lies well within the biological transparency window (NIR-I window) ranging from 650 to 950 nm, making these CPNs highly suitable for bioimaging.[43] The ratio of radical to the other monomers does not influence the emission color of the CPNs substantially (see Figure 2d). CPNs tend to exhibit lower ϕ compared to their monomers due to unavoidable quenching within the closely packed structure of the particles.[44] While our monomers exhibit ϕ of 23−32%, the CPNs in 1-propanol made from both monomers, **oct-CzBr₂-TTM** and **bisoct-CzBr₂-TTM**, exhibit increasing ϕ between 0.7 and 5.3% when raising the radical monomer ratio from 10 to 50 mol %. These values are therefore among the best for red-emitting radical nanoparticles and only second to the very high value reported for nanoprecipitated Cz-TTM nanoparticles stabilized using block copolymers.[16,44]

2.3. Photoluminescence Decay and Stability. Since conventional CPNs are less prone to photobleaching compared to particles loaded with commercial dyes,[26] we believe that this feature is also preserved for our radical dye-containing particles. Hence, we compare our radical CPNs with a loading of 50 mol % **oct-CzBr₂-TTM** to commercial polystyrene latex particles loaded with rhodamine B, with d = 500 nm. We monitor the photoluminescence of three individual particles for each sample over the course of 70 s using confocal microscopy (see Figures 3a and S2). All three latex particles bleach faster than the radical CPNs. We have calculated the irradiation dose required to reduce the original

luminescence to 50% ($D_{1/2}$). It can be clearly seen that $D_{1/2}$ of the radical CPNs is approximately twice as large as for the rhodamine-loaded polystyrene particles (see Table S1), thus confirming the superior photostability of the radical CPNs compared to commercial dye-doped polystyrene particles (see Figure 3a). This characteristic is highly important for future applications in bioimaging as high photostability enables longer and more reliable particle tracking. To test whether these particles can be taken up by cells, we incubate J774A.1 cells with the same CPNs as used for the former photostability measurements. We monitor the uptake of the red-fluorescing particles by the macrophage *via* confocal microscopy, while the cell membrane has been stained using CellBrite NIR750 (a cytoplasmic membrane dye from Biotium). The uptake of the particles by the cell begins immediately after the addition of the CPNs to the cells. We verify the successful uptake *via* confocal microscopy showing that several CPNs are located within the macrophage after only 3 h of incubation (see Figure 3b), while most studies apply an incubation time of 12−24 h before imaging.[45−48] These results confirm that the CPNs represent powerful contrast agents for fluorescence imaging with high biocompatibility.[24,26,28] Besides photostability, representing the fluorescence decay over the course of minutes due to photooxidation, we also investigate the photoluminescence lifetime of the particles. The average photoluminescence lifetimes τ_{av} are determined for the particles using a biexponential fit for the decays, as more than one decay mechanism seems to take place after photoexcitation (see Figure S3 and Table S2). While all CPNs exhibit τ_{av} in the ns range, CPNs synthesized with increasing amounts of radical comonomers exhibit a slight decrease in τ_{av} (see Figure 3c). Depending on the radical content in the particles, τ_{av} for **bisoct-CzBr₂-TTM** containing CPN are found between 6 and 7 ns, while the CPNs based on **oct-CzBr₂-TTM** exhibit τ_{av} between 2 and 3 ns (see Table S2). The shorter τ_{av} in the particles as opposed to the monomers may be a consequence of the more rigid environment, thus restricting vibrational and rotational degrees of freedom during the $D_1 \rightarrow D_0$ relaxation.

2.4. Quantum Mechanical Calculations. We perform quantum mechanical unrestricted Kohn−Sham density functional theory (UDFT) calculations and optimize the geometry of the excited D_1 and ground D_0 state. For the optimization of the D_0 geometry, we employ a uB3LYP functional with a 6-31+G* basis set.[49−52] The geometry of the D_1 state is obtained
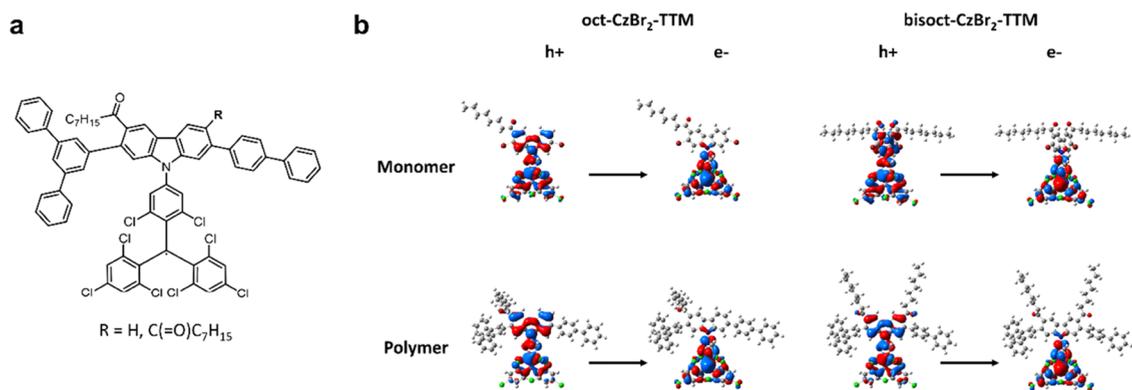
Figure 4. (a) Chemical structure of the model compound that was used for computational studies to simulate the polymeric structure within the CPNs. Depending on the open-shell monomer used for the particle synthesis, the fragment with either only one or two octanoyl groups is used. (b) Illustration of calculated electron and hole NTOs of the D1 state in **oct-CzBr$_2$-TTM** and **bisoct-CzBr$_2$-TTM** and their corresponding polymer fragments at the TD-DFT level with TDA, using an uLC-ωPBE functional and a 6-31+G** basis set.

from time-dependent DFT (TD-DFT) calculations also using a uB3LYP functional with Tamm−Dancoff approximation (TDA) and the same basis set.[53,54] The monomers show large changes in the dihedral angle between the carbazole donor and the directly connected phenyl ring of the trityl radical, when comparing the ground and the excited state (see Figure S4). This rotation will require time during the relaxation from D$_1$ → D$_0$. Successive addition of octanoyl chains to the carbazole donor leads to smaller changes in the dihedral angle between the ground and excited states and therefore during the D$_1$ → D$_0$ transition.

We attempt to show the decreased geometrical change of the radical unit in the polymer network by DFT calculations; however, this is very challenging. While the monomers can be easily modeled in our computational study, the complex structure of the polymer network within the particles is beyond the scope of such calculations. Hence, we simulate the polymeric structure using a representative fragment, as shown in Figure 4a. Depending on the open-shell monomer employed, either one or two octanoyl chains are attached to the carbazole unit. The D$_0$ and D$_1$ geometries of the two polymer fragments are obtained using the same basis sets and functionals as for the monomers. By comparing the dihedral angles between the Cz moiety and the directly connected phenyl ring of the TTM motif in the ground and excited states, the changes in geometry can be deducted for each molecule (see Table S3). The trend of smaller dihedral angles for successive octanoyl functionalization as observed in the monomers is also observed in the polymer fragments. However, within a polymer matrix, these rotations will be obstructed due to steric constraints of the surrounding polymer network, leading to reduced τ_{av} in the particles compared to the monomers. The steric hindrance that will occur in the real-world polymer network cannot be modeled here due to the linear and small nature of the employed fragment and since larger fragments would become computationally too expensive (see Table S3).

Moreover, we perform single-point calculations using the long-range corrected uLC-ωPBE functional and the 6-31+G** basis set to gain a better insight into the electronic properties of the molecules.[53] Compared to standard exchange−correlation functionals like B3LYP, the long-range-corrected uLC-ωPBE functional is supposed to deliver more accurate results for molecules in the excited CT state.[55,56] The

electronic properties of the excited states are calculated by TD-DFT calculations with TDA. These calculations confirm that the red-colored emission can only derive from the D$_1$ → D$_0$ transition, as all other electronic transitions are associated with higher energies. Hence, it can be concluded that the doublet nature is retained during the emission process. Using this functional, we are also able to depict the natural transition orbitals (NTOs) for the D$_0$ → D$_1$ transitions. It can be clearly seen that neither the monomer nor the polymer fragments exhibit a discrete CT state (see Figure 4b). As expected, the hole is located on the donor unit; however, it also spreads across the trityl moiety. By contrast, the electron is only located on the trityl unit. The electron-withdrawing octanoyl groups reduce the donor strength of the carbazole unit and therefore evoke a hybridized local and charge-transfer (HLCT) state. Interestingly, the HLCT behavior is observed in the small molecular monomer units as well as for the radicals within the polymer fragment. This similarity corroborates that the radicals behave as individual emitters and no delocalization into the conjugated backbone occurs.

2.5. Magnetic Properties of the Particles. This localization of the radical electron to the trityl TTM unit of the radical monomer is further confirmed by electron paramagnetic resonance spectroscopy (EPR). Our radical CPNs exhibit a single intense electron spin resonance signal with g values close to the free electron.[57] The peak-to-peak linewidth of the CPNs account for 7 and 10 G, respectively (see Figure S5). These rather broad signals are typical for solid samples caused by anisotropy effects. If the electron was delocalized over the carbazole unit, the interaction with the nitrogen atom would result in hyperfine splitting, which is not observed in our systems (see Figure S5).[58] This localization can be understood, when consulting the SOMO obtained from DFT calculations, where the radical electron is clearly confined to the trityl part of the small molecules and polymer fragments (see Figure S6). It has been shown that covalent organic frameworks (COFs) constructed from regularly assembled trityl radicals exhibit paramagnetic behavior due to the unpaired radical electron.[13] We now want to check, whether our amorphous arrangement of radical emitters will display similar characteristics. We determine the magnetization (M) of CPN with 50 mol % of **oct-CzBr$_2$-TTM** using a vibrating sample magnetometer (VSM) at room temperature. M increases linearly for small applied fields, while approaching
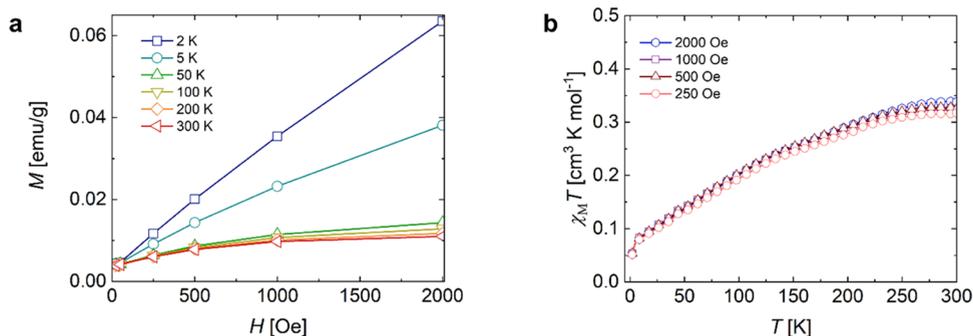
Figure 5. SQUID measurements of CNPs with an initial loading of 50 mol % **oct-CzBr$_2$-TTM** at different magnetic fields over the temperature range of 2–300 K. (a) Field-dependent magnetization of the CPNs at different temperatures. (b) Temperature-dependent magnetic susceptibilities at different applied fields.

saturation at a magnetic field of 14 000 G and a magnetic moment of ∼0.017 emu/g, indicating the paramagnetic nature of our radical CPNs (see Figure S7). However, for some trityl-based COFs, magnetic exchange coupling between the radical centers has been observed.[59,60] To ascertain whether exchange coupling is also present in our CPNs, we perform temperature-dependent magnetization studies using superconducting quantum interference magnetometry (SQUID). M is determined at various fields, while heating the sample from 2 to 300 K. Plotting M against the applied magnetic field H reveals that the same increase in magnetization as already seen for room temperature measurements is found also at a lower temperature, whereby the increase is more pronounced for low temperatures (see Figure 5a). At room temperature, the sample already approaches saturation at applied fields of 2000 Oe, which is not the case for lower temperatures. (see Figure 5a). Additionally, the temperature-dependent magnetic susceptibility ($\chi_M T$) is plotted against the temperature (T) to further elucidate the magnetic properties of the CPNs (see Figure 5b). $\chi_M T$ increases gradually when increasing T from 2 K to room temperature and saturates at a value of 0.32 cm^3 K/ mol. Unlike several other radical species, our CPNs do not undergo any change or transition within the $\chi_M T$ versus T plot, indicating the absence of strong ferromagnetic or antiferromagnetic interaction.[61] This can be further confirmed by the χ_M versus T plot, which does not exhibit a transition either and thus indicates the absence of magnetic interaction between the radical centers, confirming the paramagnetic nature of our CPNs (see Figure S8). The absence of the magnetic interaction could be due to relatively large distances between the radicals in our CPNs, allowing them to act as isolated spin centers.

3. CONCLUSIONS

We present the synthesis of monodisperse conjugated polymer nanoparticles carrying light-emitting radical units. These CPNs show exceptional optical as well as magnetic properties. Besides their high photostability and ϕ of up to 5.3% within the biological transparency window, the particles also exhibit a paramagnetic ground state induced by the unpaired electron spin. Because of these features paired with the outstanding biocompatibility of CPNs, our particles bear great potential as contrast agents for simultaneous tracking by magnetic resonance imaging and fluorescence imaging. First *in vitro* cell uptake experiments confirm their potential for biological applications. In the future, this radical CPN system will on the one hand enable more accurate diagnostics and might on the

other hand also represent interesting building blocks for quantum technological applications. The CPNs can also be surface functionalized with specific biological or supra-molecular recognition motifs for targeted imaging of pathological sites[26,62] or to enable precise self-assembly into programmed architectures.[29]

■ AUTHOR INFORMATION

Corresponding Author

Alexander J. C. Kuehne − *Institute of Organic and Macromolecular Chemistry, Ulm University, 89081 Ulm, Germany;* orcid.org/0000-0003-0142-8001; Email: alexander.kuehne@uni-ulm.de

Authors

Lisa Chen − *Institute of Organic and Macromolecular Chemistry, Ulm University, 89081 Ulm, Germany*

Tamara Rudolf − *Institute of Organic and Macromolecular Chemistry, Ulm University, 89081 Ulm, Germany*

Rémi Blinder − *Institute for Quantum Optics, Ulm University, 89081 Ulm, Germany;* orcid.org/0000-0001-6655-0150

Nithin Suryadevara − *Institute of Quantum Materials and Technologies, Karlsruhe Institute of Technology, 76344 Eggenstein-Leopoldshafen, Germany*

Ashley Dalmeida − *Institute for Functional Nanosystems, Ulm University, 89081 Ulm, Germany*

Philipp J. Welscher − *Institute of Organic and Macromolecular Chemistry, Ulm University, 89081 Ulm, Germany*

Markus Lamla − *Institute of Organic and Macromolecular Chemistry, Ulm University, 89081 Ulm, Germany*

Mona Arnold − *Institute of Organic and Macromolecular Chemistry, Ulm University, 89081 Ulm, Germany*

Ulrich Herr − *Institute for Functional Nanosystems, Ulm University, 89081 Ulm, Germany*

Fedor Jelezko − *Institute for Quantum Optics, Ulm University, 89081 Ulm, Germany*

Mario Ruben − *Institute of Quantum Materials and Technologies and Institute of Nanotechnology, Karlsruhe Institute of Technology, 76344 Eggenstein-Leopoldshafen, Germany; Centre Européen de Sciences Quantiques (CESQ), Institut de Science et d'Ingénierie Supramoléculaires (ISIS), 67083 Strasbourg, France*

■ REFERENCES

(1) Abdurahman, A.; Hele, T. J. H.; Gu, Q.; Zhang, J.; Peng, Q.; Zhang, M.; Friend, R. H.; Li, F.; Evans, E. W. Understanding the Luminescent Nature of Organic Radicals for Efficient Doublet Emitters and Pure-Red Light-Emitting Diodes. *Nat. Mater.* **2020**, *19*, 1224−1229.

(2) Ballester, M.; de la Fuente, G. Synthesis and Isolation of a Perchlorotriphenylcarbanion Salt. *Tetrahedron Lett.* **1970**, *11*, 4509−4510.

(3) Armet, O.; Veciana, J.; Rovira, C.; Riera, J.; Castañer, J.; Molins, E.; Rius, J.; Miravitlles, C.; Olivella, S.; Brichfeus, J. Inert Carbon Free Radicals. 8. Polychlorotriphenylmethyl Radicals. Synthesis, Structure, and Spin-Density Distribution. *J. Phys. Chem. A* **1987**, *91*, 5608−5616.

(4) Sholle, V. D.; Rozantsev, E. G. Advances in the Chemistry of Stable Hydrocarbon Radicals. *Russ. Chem. Rev.* **1973**, *42*, 1011−1019.

(5) Peng, Q.; Obolda, A.; Zhang, M.; Li, F. Organic Light-Emitting Diodes Using a Neutral π Radical as Emitter: The Emission from a Doublet. *Angew. Chem., Int. Ed.* **2015**, *54*, 7091−7095.

(6) Guo, H.; Peng, Q.; Chen, X.; Gu, Q.; Dong, S.; Evans, E. W.; Gillett, A. J.; Ai, X.; Zhang, M.; Credgington, D.; Coropceanu, V.; Friend, R. H.; Brédas, J.; Li, F. High Stability and Luminescence Efficiency in Donor−Acceptor Neutral Radicals Not Following the Aufbau Principle. *Nat. Mater.* **2019**, *18*, 977−984.

(7) Ai, X.; Evans, E. W.; Dong, S.; Gillett, A. J.; Guo, H.; Chen, Y.; Hele, T. J. H.; Friend, R. H.; Li, F. Efficient Radical-Based Light-Emitting Diodes with Doublet Emission. *Nature* **2018**, *563*, 536−540.

(8) Mas-Torrent, M.; Crivillers, N.; Mugnaini, V.; Ratera, I.; Rovira, C.; Veciana, J. Organic Radicals on Surfaces: Towards Molecular Spintronics. *J. Mater. Chem.* **2009**, *19*, 1691−1695.

(9) Tesio, A. Y.; Blasi, D.; Olivares-Marín, M.; Ratera, I.; Tonti, D.; Veciana, J. Organic Radicals for the Enhancement of Oxygen Reduction Reaction in Li-O2 Batteries. *Chem. Commun.* **2015**, *51*, 17623−17626.

(10) Reig, M.; Gozálvez, C.; Jankauskas, V.; Gaidelis, V.; Grazulevicius, J. V.; Fajarí, L.; Juliá, L.; Velasco, D. Stable All-Organic Radicals with Ambipolar Charge Transport. *Chem. − Eur. J.* **2016**, *22*, 18551−18558.

(11) Maspoch, D.; Ruiz-Molina, D.; Wurst, K.; Domingo, N.; Cavallini, M.; Biscarini, F.; Tejada, J.; Rovira, C.; Veciana, J. A Nanoporous Molecular Magnet with Reversible Solvent-Induced Mechanical and Magnetic Properties. *Nat. Mater.* **2003**, *2*, 190−195.

(12) Datcu, A.; Roques, N.; Jubera, V.; Maspoch, D.; Fontrodona, X.; Wurst, K.; Imaz, I.; Mouchaham, G.; Sutter, J. P.; Rovira, C.; Veciana, J. Three-Dimensional Porous Metal-Radical Frameworks Based on Triphenylmethyl Radicals. *Chem. − Eur. J.* **2012**, *18*, 152−162.

(13) Jiang, Y.; Oh, I.; Joo, S. H.; Buyukcakir, O.; Chen, X.; Lee, S. H.; Huang, M.; Seong, W. K.; Kim, J. H.; Rohde, J. U.; Kwak, S. K.; Yoo, J. W.; Ruoff, R. S. Organic Radical-Linked Covalent Triazine Framework with Paramagnetic Behavior. *ACS Nano* **2019**, *13*, 5251−5258.

(14) Cui, X.; Lu, G.; Dong, S.; Li, S.; Xiao, Y.; Zhang, J.; Liu, Y.; Meng, X.; Li, F.; Lee, C.-S. Stable π-Radical Nanoparticles as Versatile Photosensitizers for Effective Hypoxia-Overcoming Photodynamic Therapy. *Mater. Horiz.* **2021**, *8*, 571−576.

(15) Blasi, D.; Nikolaidou, D. M.; Terenziani, F.; Ratera, I.; Veciana, J. Excimers from Stable and Persistent Supramolecular Radical-Pairs in Red/NIR-Emitting Organic Nanoparticles and Polymeric Films. *Phys. Chem. Chem. Phys.* **2017**, *19*, 9313−9319.

(16) Bai, X.; Tan, W.; Abdurahman, A.; Li, X.; Li, F. Stable Red Nanoparticles Loaded Neutral Luminescent Radicals for Fluorescence Imaging. *Dyes Pigm.* **2022**, *202*, No. 110260.

(17) Wu, C.; Peng, H.; Jiang, Y.; McNeill, J. Energy Transfer Mediated Fluorescence from Blended Conjugated Polymer Nanoparticles. *J. Phys. Chem. B* **2006**, *110*, 14148−14154.

(18) MacFarlane, L. R.; Shaikh, H.; Garcia-Hernandez, J. D.; Vespa, M.; Fukui, T.; Manners, I. Functional Nanoparticles through π-Conjugated Polymer Self-Assembly. *Nat. Rev. Mater.* **2021**, *6*, 7−26.

(19) Sarrazin, P.; Chaussy, D.; Vurth, L.; Stephan, O.; Beneventi, D. Surfactant (TTAB) Role in the Preparation of 2,7-Poly (9,9-Dialkylfluorene- Co-Fluorenone) Nanoparticles by Miniemulsion. *Langmuir* **2009**, *25*, 6745−6752.

(20) Reese, C. E.; Asher, S. A. Emulsifier-Free Emulsion Polymerization Produces Highly Charged, Monodisperse Particles for near Infrared Photonic Crystals. *J. Colloid Interface Sci.* **2002**, *248*, 41−46.

(21) Kang, S.; Yoon, T. W.; Kim, G. Y.; Kang, B. Review of Conjugated Polymer Nanoparticles: From Formulation to Applications. *ACS Appl. Nano Mater.* **2022**, *5*, 17436−17460.

(22) Kuehne, A. J. C.; Gather, M. C.; Sprakel, J. Monodisperse Conjugated Polymer Particles by Suzuki-Miyaura Dispersion Polymerization. *Nat. Commun.* **2012**, *3*, No. 1087.

(23) Ciftci, S.; Kuehne, A. J. C. Monodisperse Conjugated Polymer Particles via Heck Coupling - A Kinetic Study to Unravel Particle Formation in Step-Growth Dispersion Polymerization. *Macromolecules* **2015**, *48*, 8389−8393.

(24) Jansen, F.; Schuster, P. A.; Lamla, M.; Trautwein, C.; Kuehne, A. J. C. Biodegradable Polyimidazole Particles as Contrast Agents Produced by Direct Arylation Polymerization. *Biomacromolecules* **2021**, *22*, 5065−5073.

(25) Kuehne, A. J. C.; Weitz, D. A. Highly Monodisperse Conjugated Polymer Particles Synthesized with Drop-Based Microfluidics. *Chem. Commun.* **2011**, *47*, 12379−12381.

(26) Anwar, N.; Rix, A.; Lederle, W.; Kuehne, A. J. C. RGD-Decorated Conjugated Polymer Particles as Fluorescent Biomedical

Probes Prepared by Sonogashira Dispersion Polymerization. *Chem. Commun.* **2015**, *51*, 9358–9361.

(27) Ciftci, S.; Jansen, F.; Chimisso, V.; Kler, J.; Rahimi, K.; Kuehne, A. J. C. Horner-Wadsworth-Emmons Dispersion Polymerization for the Production of Monodisperse Conjugated Polymer Particles under Ambient Conditions. *Polym. Chem.* **2018**, *9*, 2428–2433.

(28) Repenko, T.; Rix, A.; Ludwanowski, S.; Go, D.; Kiessling, F.; Lederle, W.; Kuehne, A. J. C. Bio-Degradable Highly Fluorescent Conjugated Polymer Nanoparticles for Bio-Medical Imaging Applications. *Nat. Commun.* **2017**, *8*, No. 470.

(29) Mikosch, A.; Ciftci, S.; Kuehne, A. J. C. Colloidal Crystal Lasers from Monodisperse Conjugated Polymer Particles via Bottom-Up Coassembly in a Sol-Gel Matrix. *ACS Nano* **2016**, *10*, 10195–10201.

(30) Piok, T.; Gamerith, S.; Gadermaier, C.; Plank, H.; Wenzl, F. P.; Patil, S.; Montenegro, R.; Kietzke, T.; Neher, D.; Scherf, U.; Landfester, K.; List, E. J. W. Organic Light-Emitting Devices Fabricated from Semiconducting Nanospheres. *Adv. Mater.* **2003**, *15*, 800–804.

(31) Rahim, N. A. A.; McDaniel, W.; Bardon, K.; Srinivasan, S.; Vickerman, V.; So, P. T. C.; Moon, J. H. Conjugated Polymer Nanoparticles for Two-Photon Imaging of Endothelial Cells in a Tissue Model. *Adv. Mater.* **2009**, *21*, 3492–3496.

(32) Wu, C.; Bull, B.; Christensen, K.; McNeill, J. Ratiometric Single-Nanoparticle Oxygen Sensors for Biological Imaging. *Angew. Chem., Int. Ed.* **2009**, *48*, 2741–2745.

(33) Kietzke, T.; Neher, D.; Landfester, K.; Montenegro, R.; Güntner, R.; Scherf, U. Novel Approaches to Polymer Blends Based on Polymer Nanoparticles. *Nat. Mater.* **2003**, *2*, 408–412.

(34) Kushida, S.; Braam, D.; Dao, T. D.; Saito, H.; Shibasaki, K.; Ishii, S.; Nagao, T.; Saeki, A.; Kuwabara, J.; Kanbara, T.; Kijima, M.; Lorke, A.; Yamamoto, Y. Conjugated Polymer Blend Microspheres for Efficient, Long-Range Light Energy Transfer. *ACS Nano* **2016**, *10*, 5543–5549.

(35) Ariu, M.; Lidzey, D. G.; Sims, M.; Cadby, A. J.; Lane, P. A.; Bradley, D. D. C. The Effect of Morphology on the Temperature-Dependent Photoluminescence Quantum Efficiency of the Conjugated Polymer Poly(9, 9-Dioctylfluorene). *J. Phys.: Condens. Matter* **2002**, *14*, 9975–9986.

(36) Díaz-García, M. A.; Hide, F.; Schwartz, B. J.; Andersson, M. R.; Pei, Q.; Heeger, A. J. Plastic Lasers: Semiconducting Polymers as a New Class of Solid-State Laser Materials. *Synth. Met.* **1997**, *84*, 455–462.

(37) Andrew, T. L.; Swager, T. M. Reduced Photobleaching of Conjugated Polymer Films through Small Molecule Additives. *Macromolecules* **2008**, *41*, 8306–8308.

(38) Chen, L.; Arnold, M.; Kittel, Y.; Blinder, R.; Jelezko, F.; Kuehne, A. J. C. 2,7-Substituted N-Carbazole Donors on Tris(2,4,6-Trichlorophenyl)Methyl Radicals with High Quantum Yield. *Adv. Opt. Mater.* **2022**, No. 2102101.

(39) Lovell, T. C.; Colwell, C. E.; Zakharov, L. N.; Jasti, R. Symmetry Breaking and the Turn-on Fluorescence of Small, Highly Strained Carbon Nanohoops. *Chem. Sci.* **2019**, *10*, 3786–3790.

(40) Shavaleev, N. M.; Eliseeva, S. V.; Scopelliti, R.; Bünzli, J. C. G. Influence of Symmetry on the Luminescence and Radiative Lifetime of Nine-Coordinate Europium Complexes. *Inorg. Chem.* **2015**, *54*, 9166–9173.

(41) Haehnle, B.; Jathavedan, K. K.; Schuster, P. A.; Karg, M.; Kuehne, A. J. C. Elucidating the Nucleation Event in the C-C Cross-Coupling Step-Growth Dispersion Polymerization. *Macromolecules* **2021**, *54*, 6085–6089.

(42) Abe, M. *Measurement Techniques and Practices of Colloid and Interface Phenomena*, 1st ed.; Abe, M., Ed.; Springer: Singapore, 2019; pp 65–70.

(43) Li, C.; Chen, G.; Zhang, Y.; Wu, F.; Wang, Q. Advanced Fluorescence Imaging Technology in the Near-Infrared-II Window for Biomedical Applications. *J. Am. Chem. Soc.* **2020**, *142*, 14789–14804.

(44) Haehnle, B.; Schuster, P. A.; Chen, L.; Kuehne, A. J. C. All-Conjugated Polymer Core − Shell and Core − Shell − Shell Particles

with Tunable Emission Profiles and White Light Emission. *Small* **2021**, *17*, No. 2101411.

(45) Mutzke, E.; Chomyshyn, E.; Nguyen, K. C.; Blahoianu, M.; Tayabali, A. F. Phagocytosis-Coupled Flow Cytometry for Detection and Size Discrimination of Anionic Polystyrene Particles. *Anal. Biochem.* **2015**, *483*, 40–46.

(46) Kim, S.; Oh, W. K.; Jeong, Y. S.; Hong, J. Y.; Cho, B. R.; Hahn, J. S.; Jang, J. Cytotoxicity of, and Innate Immune Response to, Size-Controlled Polypyrrole Nanoparticles in Mammalian Cells. *Biomaterials* **2011**, *32*, 2342–2350.

(47) Fernando, L. P.; Kandel, P. K.; Yu, J. B.; McNeill, J.; Ackroyd, P. C.; Christensen, K. A. Mechanism of Cellular Uptake of Highly Fluorescent Conjugated Polymer Nanoparticles. *Biomacromolecules* **2010**, *11*, 2675–2682.

(48) Susnik, E.; Taladriz-Blanco, P.; Drasler, B.; Balog, S.; Petri-Fink, A.; Rothen-Rutishauser, B. Increased Uptake of Silica Nanoparticles in Inflamed Macrophages but Not upon Co-Exposure to Micron-Sized Particles. *Cells* **2020**, *9*, No. 2099.

(49) Parr, R. G.; Yang, W. *Density Functional Theory of Atoms and Molecules*; Oxford University Press: USA, 1989.

(50) Kohn, W.; Sham, L. J. Self-Consistent Equations Incouding Exchange and Correlation Effects. *Phys. Rev.* **1965**, *140*, A1133–A1139.

(51) Becke, A. D. A New Mixing of Hartree-Fock and Local Density-Functional Theories. *J. Chem. Phys.* **1993**, *98*, 1372–1377.

(52) Stephen, P. J.; Devlin, F. J.; Chabalowski, C. F.; Frisch, M. J. Ab Initio Calculation of Vibrational Absorption. *J. Phys. Chem. B* **1994**, *98*, 11623–11627.

(53) Vydrov, O. A.; Scuseria, G. E. Assessment of a Long-Range Corrected Hybrid Functional. *J. Chem. Phys.* **2006**, *125*, 234109.

(54) Hirata, S.; Head-Gordon, M. Time-Dependent Density Functional Theory within the Tamm-Dancoff Approximation. *Chem. Phys. Lett.* **1999**, *314*, 291–299.

(55) Tsuneda, T.; Hirao, K. Long-Range Correction for Density Functional Theory. *Wiley Interdiscip. Rev. Comput. Mol. Sci.* **2014**, *4*, 375–390.

(56) Dreuw, A.; Head-Gordon, M. Failure of Time-Dependent Density Functional Theory for Long-Range Charge-Transfer Excited States: The Zincbacteriochlorin− Bacteriochlorin and Bacteriochlorophyll-Spheroidene Complexes. *J. Am. Chem. Soc.* **2004**, *126*, 4007–4016.

(57) Wilkinson, D. T.; Crane, H. R. Precision Measurement of the g Factor of the Free Electron. *Phys. Rev.* **1963**, *130*, 852–863.

(58) Griffith, O. H.; Waggoner, A. S. Nitroxide Free Radicals: Spin Labels for Probing Biomolecular Structure. *Acc. Chem. Res.* **1969**, *2*, 17–24.

(59) Yang, Y.; Liu, C.; Xu, X.; Meng, Z.; Tong, W.; Ma, Z.; Zhou, C.; Sun, Y.; Sheng, Z. Antiferromagnetism in Two-Dimensional Polyradical Nanosheets. *Polym. Chem.* **2018**, *9*, 5499–5503.

(60) Wu, S.; Li, M.; Phan, H.; Wang, D.; Herng, T. S.; Ding, J.; Lu, Z.; Wu, J. Toward Two-Dimensional π-Conjugated Covalent Organic Radical Frameworks. *Angew. Chem., Int. Ed.* **2018**, *57*, 8007–8011.

(61) Kumar, S.; Kumar, Y.; Keshri, S. K.; Mukhopadhyay, P. Recent Advances in Organic Radicals and Their Magnetism. *Magnetochemistry* **2016**, *2*, No. 42.

(62) Repenko, T.; Rix, A.; Ludwanowski, S.; Go, D.; Kiessling, F.; Lederle, W.; Kuehne, A. J. C. Bio-Degradable Highly Fluorescent Conjugated Polymer Nanoparticles for Bio-Medical Imaging Applications. *Nat. Commun.* **2017**, *8*, No. 470.